Critical Effect of Carbon Vacancies on the Reverse Water Gas Shift Reaction over Vanadium Carbide Catalysts

Arturo Pajares[a,b,¶], Hèctor Prats[c,¶], Alexandre Romero[d], Francesc Viñes[c,*], Pilar Ramírez de la Piscina[a,*], Ramon Sayós[c], Narcís Homs[a,b], and Francesc Illas[c]

[a]*Departament de Química Inorgànica i Orgànica, Secció de Química Inorgànica and Institut de Nanociència i Nanotecnologia (IN2UB), Universitat de Barcelona, Martí i Franquès 1-11, 08028 Barcelona, Spain.*

[b]*Catalonia Institute for Energy Research (IREC), Jardins de les Dones de Negre 1, 08930 Barcelona, Spain*

[c]*Departament de Ciència de Materials i Química Física & Institut de Química Teòrica i Computacional (IQTCUB), Universitat de Barcelona, Martí i Franquès 1-11, 08028 Barcelona, Spain.*

[d]*École Nationale Supérieure des Ingénieurs en Arts Chimiques et Technologiques (INP-ENSIACET), 4 Allée Emile Monso, 31030 Toulouse, France.*

[*] Corresponding authors: Francesc Viñes (francesc.vines@ub.edu), Pilar Ramírez de la Piscina (pilar.piscina@qi.ub.edu)

Keywords: vanadium carbide; carbon vacancies; reverse water gas shift; CO_2 utilization, heterogeneous catalysis; density functional calculations

ABSTRACT

Experimental and theoretical evidences show that carbon vacancies determine the catalytic behavior of vanadium carbides in the CO_2 conversion to CO *via* the Reverse Water Gas Shift (RWGS) reaction. Two VC_x samples, one mostly containing stoichiometric VC and the other being C deficient, mainly V_8C_7, were synthesized, characterized, and studied. The samples show different CO_2 adsorption heats, which correlate with those calculated using Density Functional Theory (DFT) on suitable models. The sample containing more V_8C_7 shows a higher CO_2 conversion and CO selectivity and a lower apparent activation energy, being a stable catalyst over long-time tests. DFT calculations confirm that C vacancies in V_8C_7 are responsible for the observed catalytic behavior, allowing reactants to adsorb more strongly, lowering the energy barrier for both H_2 and CO_2 dissociation steps. The present work highlights the importance of such native point defects in the transition metal carbides surface chemistry and catalytic properties.

1. Introduction

The industrial utilization of CO_2 as a carbon source for chemical processes is appealing from the environmental point of view, with obvious benefits removing the main greenhouse gas causing global warming and, at the same time, constituting an abundant and cheap C_1 chemical feedstock. Thus, it is no strange that, nowadays, great research endeavors are addressed towards the CO_2 chemistry, with emphasis on the chemical conversion of CO_2 by heterogeneous catalysis [1]. However, this overall process requires materials able to capture the gas CO_2, through the so-known Carbon Capture and Storage (CCS) technologies [2,3]. Ideally, such a scrubber material would not only sequester CO_2 but as well promote its chemical activation thus constituting a possible useful candidate material for Carbon Capture and Utilization (CCU) technologies [2-5], allowing a simplified potential industrial setup. Along these lines, the Reverse Water Gas Shift (RWGS) reaction ($CO_2 + H_2 \rightarrow CO + H_2O$; $\Delta_r H^o = 41.2$ kJ mol^{-1} —0.43 eV— at 298 K) [6] has gained momentum towards the utilization of CO_2 as an economic C_1 carbon source, *e.g.* for synthetic fuel production [7]. After water separation, the RWGS generated CO can be used, within a $CO/CO_2/H_2$ mixture, as synthesis gas (*syngas*) for the Fischer-Tropsch or methanol synthesis to obtain hydrocarbons and/or alcohol fuels [8]. Within these premises, the RWGS coupled to a sustainable source of energy for the reaction requirements —*i.e.* renewable H_2 production— could be introduced as a fundamental gear to close the C-cycle.

Recently, Density Functional Theory (DFT) based calculations have predicted that early Transition Metal Carbides (TMCs) are possible highly-active, resilient, and economic materials for CCS technologies, even at stringent conditions of temperature and CO_2 partial pressure [9]. Such TMCs are long-regarded in the literature as alternative materials to Pt-group transition metal-based catalysts, with similar or even higher catalytic activities and selectivities [10], very high chemical and physical resistances [11], and even being typically S- and C-poisoning resistant [12-15]. At variance with Pt-group transition metals, the strong CO_2 adsorption on the different TMCs can even allow their use in chemical resolution processes, such as the separation of CH_4 and CO_2 in biogas upgrading processes [16]. These computational simulations forecasted that some of these TMCs, such as ZrC and HfC, would be able to capture CO_2 even at 473 K from sources with a low CO_2 content, such as atmospheric air, with a current CO_2 partial pressure, p_{CO_2}, of 40.5 Pa [17]. The theoretical predictions became afterwards experimentally confirmed on TiC, ZrC, and VC samples [18]. Further, several TMCs were found to be able to activate CO_2, resulting in a partially negatively charged bent molecular species. This added up to the point that such TMCs are able to

attach H_2 and split it [19-21], allows considering them as viable catalysts for CO_2 hydrogenation reactions [22].

In principle, activated CO_2 can evolve to CO although this constitutes the main rate-limiting step of the RWGS. In this context, several TMCs have been proposed as economic alternative catalysts to current Pt/CeO_2 for the RWGS [23] since TMCs materials seem to be able to reduce the CO_2 dissociation step energy barrier [24]. From a theoretical point of view, δ-MoC and α- and β-Mo_2C have been the most studied TMCs for CO_2 reduction [24-27], where the Mo:C ratio has been often argued as being a critical aspect of the material surface chemistry and catalytic behaviour [28,29]. Similarly, in a recent study, the W:C ratio of tungsten carbides embedded in carbon spheres ($W_xC@CS$) was found to directly affect the guaiacol to phenol production and selectivity by hydrogenolysis [30]. Even though TMCs are known to display a certain quantity of C vacancies, up to the point that sub-stoichiometric phases are common [31,32], most of the previous catalytic studies dealt with idealized stoichiometric TMC phases. Inspired by the key role that oxygen vacancies play in the catalytic behaviour of transition metal oxides [33,34], and by recent findings showing that the Strong Metal Support Interaction (SMSI) concept [35,36] can be extended from metal/oxide to metal/carbide catalysts [37], disclosing the effects that C vacancies may have on the catalytic behaviour of TMCs appears mandatory. In this respect, it has been claimed that, given the difficulty of gaining the significance of defect chemistry in TMCs by solely experimental studies [38], theoretical simulations constitute a complementary powerful tool.

Here, a combination of experiments and computational models are applied to the study of the mechanism of the RWGS catalysed by vanadium carbide. VC has been selected because, compared to other TMCs, it displays a low affinity for oxygen [39-41], thus preventing the easy formation of oxycarbides. Furthermore, earlier DFT calculations showed that the hybridization between V d and C p orbitals yields hydrogen binding energies comparable to Mo_2C and WC yet slightly smaller [19,22,42]. The small O affinity of VC anticipates a poor RWGS catalytic activity, destabilizing the adsorbed O adatom intermediate state formed during the CO_2 reduction to CO. Surprisingly, VC_x samples, here prepared using a novel *sol-gel* method, reveal a good catalytic performance in the RWGS reaction. This unforeseen behaviour is here explained on the basis of reaction profiles obtained from DFT-based calculations revealing the key role played by surface C vacancies. Interestingly, this reaction is barely feasible when C vacancies are not present. In short, the present work provides compelling evidence of the paramount role that C vacancies have in determining the surface chemistry and the concomitant catalytic behaviour of VC, likely to affect the chemistry of other TMC materials. Thus, the present findings highlight the importance of such native point defects in determining the overall chemistry and catalytic properties of TMC surfaces,

showing how and why the presence of vacancies completely determines the resulting catalytic behaviour.

2. Experimental Section

2.1. Catalyst preparation

We studied the preparation of VC_x phases applying a gel-like method and using 4,5-dicyanoimidazole as carbon precursor and $VOCl_3$ or $VO(isopropoxide)_3$ as vanadium precursors. A summary of the synthesis is given in Section S1 of the Supplementary Material. Among all the prepared samples, VC-1 and VC-2 were specifically chosen for this work. Briefly, for the preparation of VC-1, 7.96 mmol of $VOCl_3$ were dissolved into 15 mL of ethanol, and then 7.96 mmol of 4,5-dicyanoimidazole were added. The solution was kept under continuous stirring at room temperature under Ar and afterwards ethanol was evaporated to produce a gel. The sample was treated in a tubular furnace under Ar flow up to 1373 K (2.5 $K \cdot min^{-1}$) for 5 h; then cooled down to room temperature under Ar and exposed to room ambient without passivation. The VC-2 sample was similarly prepared using 7.96 mmol of $VO(isopropoxide)_3$ and 10.75 mmol of 4,5-dicyanoimidazole. The preparation method used is inspired in the soft-urea pathway but using 4,5-dicyanoimidazole as carbon source [43]. The initial gel condenses during the thermal treatment with the formation of an intermediate glass. The composition of this intermediate material, which depends on the metal and carbon precursors and the carbon precursor/metal precursor ratio, is expected to influence the final material obtained [43,44]. After preparation, samples were not passivated because a detrimental effect of the O_2 passivation in the activity of alumina-supported molybdenum carbide catalysts for CO_2 hydrogenation has been found [45]. It seems that is easier to control the extent of oxidation when mild oxidants such as CO_2 or H_2O are used [46,47].

2.2. Characterization

N_2 adsorption-desorption isotherms were carried out at 77 K using a Micromeritics Tristar II 3020 instrument. The specific surface area (S_{BET}) was calculated by multipoint analysis of N_2 adsorption isotherms. The pore size distribution was calculated applying the BJH method. Powder X-ray diffraction patterns (XRD) were collected between $2\theta = 20°\text{-}100°$, with a step width of 0.017° and counting 80 s at each step, using a PANalytical X'Pert PRO MPD Alpha1 powder diffractometer, focalizing Ge (111) primary monochromator and Cu Kα1 radiation source ($\lambda = 1.5406$ Å). The mean crystallite size of VC_x phases were calculated using the Debye-Scherrer equation. Scanning Transmission Electron Microscopy (STEM) images were acquired using a JEOL JEM-2100 LaB6

transmission electron microscope, operating at 200 kV in STEM mode, using the high angle annular dark field detector; the beam size was around 15 nm. Energy Dispersive X-ray (EDX) analysis was performed with an Oxford Instruments INCA x-sight, with Si (Li) detector coupled to the STEM system. Map acquisition was accomplished using the INCA Microanalysis Suite version 4.09 software.

Transmission Electron Microscopy (TEM) images and the phase mapping of samples were collected employing a JEOL J2010F microscope operated at an accelerating voltage up to 200 kV. To obtain a reliable phase map at the nanometric scale we used the electron beam precession in TEM analysis together with spot Precession Electron Diffraction (PED) pattern recognition, commercial ASTAR^{TM} technique [48-50]. Maps were acquired using a step size of 5 or 10 nm. The precession unit was operated at 100 Hz, acquiring 5 frames per second and using a precession angle of 1°. PED patterns were recorded with an ultrafast external camera (Stingray F-046 Allied Visions) and used for the crystal phase mapping construction. The distortions in the diffraction patterns introduced by the external position of the camera were corrected during the data treatment.

H$_2$-Temperature Programmed Reduction (H$_2$-TPR) experiments were carried out using a Micromeritics AutoChem II 2920 chemisorption equipment. Samples were pretreated at 363 K under He and then, exposed to a H$_2$/Ar (12% v/v) flow, the temperature was increased up to 1073 K at 10 K·min^{-1}. X-ray Photoelectron Spectroscopy (XPS) analysis was performed using a Perkin Elmer PHI-5500 Multitechnique System (Physical Electronics) with an Al X-ray source (hν = 1486.6 eV and 350 W). Samples were kept in an ultra-high vacuum chamber during data acquisition (5·10^{-9}-2·10^{-8} Torr). Using Au as reference, the Binding Energy (BE) of C 1s at 284.8 eV, attributed to adventitious carbon, was determined. This signal was used as reference for the determination of all the others BE values. Raman spectra were collected using a Jobin-Yvon LabRam HR 800, with an optical Olympus BXFM microscope, a 532 nm laser and a CCD detector. The laser power was limited to 0.75 mW to reduce laser-heating effects during spectra acquisition.

Thermogravimetric and calorimetric analysis, applied to study the CO$_2$ adsorption onto the catalysts and the reactivity of CO$_2$ with the catalysts, were carried out using a Sensys Evo TG-DSC instrument (Setaram), equipped with a 3D thermal flow sensor, coupled to a Pfeiffer Mass Spectrometer (MS). For CO$_2$ adsorption, catalysts (50 mg) were firstly dried in Ar flow at 353 K, then heated up to 823 K (10 K·min^{-1}) under a H$_2$/Ar flow (10% v/v) for 1 h, and finally cooled down to 303 K for CO$_2$ chemisorption. In separate experiments, the reactivity of catalysts with CO$_2$ was studied at 873 K. Dry samples were heated up to 873 K at 10 K·min^{-1} under flowing CO$_2$/Ar (10% v/v); then, after 3 h at 873 K, cooled down at room temperature, and further characterized. The presence of CO in the outflow was determined by MS analysis.

2.3. RWGS catalytic tests

RWGS tests were performed in a Microactivity-Reference unit (PID Eng&Tech). A tubular fixed-bed 316-L stainless steel reactor (305 mm long, 9 mm i.d,) with a thermocouple in direct contact with the catalytic bed was used. In all cases, 150 mg of catalyst and a catalytic bed of 1 mL were utilized; silicon carbide was used as diluting agent. The fresh catalyst was heated from room temperature up to 573 K under N_2 flow and then, exposed to a reactant gas mixture of CO_2/H_2/N_2 = 1/3/1 (mol/mol) under a Gas Hourly Space Velocity (GHSV) of 3000 h^{-1}. The catalytic behavior in the RWGS was studied between 573 K and 873 K at 0.1 MPa. The long-term catalytic test (about four days) was carried out at 723 K, using 300 mg of catalyst and keeping all the other reaction conditions. The products were analyzed online with a Varian 450-GC-MS equipped with a TCD, two FID and a mass detector. Only CO and CH_4 were found as products. The carbon balance between the outlet gas and the reactant inlet was ≤ 1%. CO_2 conversion and product distribution were determined at each temperature by the average of at least 4 different analyses. The CO_2 conversion (X_{CO_2}) and the selectivity to the *i* product (S_i) were defined and obtained as follows:

$$X_{CO_2}(\%) = \left(1 - \frac{(C_{CO_2})_{outlet}}{(C_{CO_2})_{outlet} + \sum(C_i)_{outlet}}\right) \cdot 100 \qquad (1),$$

$$S_i(\%) = \frac{(C_i)_{outlet}}{\sum(C_i)_{outlet}} \cdot 100 \qquad (2),$$

where (C_i) and C_{CO_2} are the molar concentration of the *i* product (CO or CH_4) and CO_2, respectively.

3. Computational methods

Periodic spin-polarized DFT based calculations have been carried out using the Vienna *Ab Initio* Simulation Package (VASP) code [51]. The Perdew-Burke-Ernzerhof (PBE) exchange-correlation (*xc*) functional has been chosen [52], and dispersion —van der Waals— interactions have been included through the D3 method as proposed by Grimme and coworkers [53]. The PBE-D3 calculated energy differences are accurate enough to properly describe the interaction of reactants, intermediates, and products on TMC systems, as proven in the past on joint experimental and theoretical works [18-20,24,27]. The valence electron density has been expanded in a plane wave basis set with a kinetic energy cutoff of 415 eV. The effect of core electrons on the valence electron density is described by the Projector Augmented Wave (PAW) method of Blöchl [54], as

implemented by Kresse and Joubert [55]. The gas-phase energy of a species i, E_i, is gained by placing the gas molecule and optimizing its structure in an asymmetric box of 9×10×11 Å at the Γ-point. A 9×9×1 Monkhorst-Pack [56] scheme **k**-point mesh has been used in all the slab calculations, whose geometries have been optimized prior to the placing of any adsorbate. Initial guesses for adsorbate geometries were obtained by placing the adsorbate at different sites, see Figure 1.

The surface slab models have been constructed for the VC(001) surface, experimentally known to be the most stable and, hence, dominant surface in samples of rocksalt TMCs, but also confirmed based on theoretical estimates of surface energies, which point out such surface being, to a large extent, the most exposed, as expected from the Wulff construction minimizing the overall material surface tension [11,57,58]. The slab models have been built from a previously optimized bulk unit cell and contain four atomic layers, where the bottom two have been constrained to bulk positions to provide the appropriate environment to the two uppermost surface atomic layers, whose atomic structure has been fully relaxed [9]. To avoid interactions between the periodically interleaved slabs, a vacuum region of 12 Å perpendicular to the surface has been added. The structure of all adsorbates has been relaxed to find their optimum geometry using a conjugate-gradient algorithm, with an energy convergence criterion for electronic updates of 10^{-5} eV, and an atomic force convergence criterion of 0.02 eV Å^{-1}. The optimized geometries have been characterized as minima in the potential energy surface by frequency analysis with 0.03 Å finite displacements.

The VC(001) surface slab model used in the present work consists of a (2√2×2√2)R45º surface unit cell, having a total of 32 V and 32 C atoms, see Figure 1 whereas a second system corresponding to VC(001) with a surface C vacancy, labelled VC-vac, was constructed to model the $V_8C_7(001)$ phase. This choice is reasonable, since the optimized lattice parameters for both VC and V_8C_7 are identical. The only difference among these bulk structures arises from the presence of extra C vacancies in V_8C_7 at the subsurface and inner layers in an ordered manner. However, the C-defective sites at the surface are the only ones strongly affecting the catalytic properties of the material. Therefore, adsorption energies and energy barriers on V_8C_7 can be obtained from a system consisting on VC with a surface C vacancy. Further details regarding the validity of using VC(001) with a surface C vacancy to model the $V_8C_7(001)$ are provided in the Supplementary Material, section S2, Figures S1 and S2 and Table S1. For final geometries, the adsorption energy of a species i, $\Delta_{ads}E_A^{ZPE}$, is then calculated as:

$$\Delta_{ads}E_i^{ZPE} = E_{i,slab} - (E_{slab} + E_i) + E_{ZPE} \tag{3},$$

where $E_{i,slab}$ is the energy of the species i adsorbed on the corresponding slab model, E_{slab} is the energy of the relaxed pristine slab, E_i is the energy of an isolated molecule of species i, and E_{ZPE} is the Zero Point Energy (ZPE) term, calculated considering both gas phase and adsorbed phase within the harmonic approximation, with Hessian matrix elements obtained from finite differences of analytical gradients with displacements of 0.03 Å.

Finally, Transition State (TS) structures were located by using the Climbing-Image Nudged Elastic Band (CI-NEB) method [59]. The initial guesses for the employed four intermediate images were generated by means of the Atomic Simulation Environment (ASE) [60] package using the Image Dependent Pair Potential (IDPP) procedure [61]. The obtained TS candidates have been characterized by a proper vibrational analysis, *vide supra*. The potential energy reaction profiles correspond to 0 K and in vacuum pressure conditions. To account for temperature and pressure effects, the free energy reaction profiles have been acquired at the catalytic working conditions of temperature (873 K) and reactant pressures (p_{CO_2} = 20 kPa, p_{H_2} = 60 kPa) by using the atomistic statistical thermodynamics approach [62], see details in the Supplementary Material.

4. Results and discussion

Both VC-1 and VC-2 are mesoporous materials with average pore widths of 5.0 and 3.4 nm, and S_{BET} of 204 and 315 m^2 g^{-1}, respectively. The XRD analysis (see Figure S3) indicates the presence of cubic VC (JCPDS 01-073-0476) and/or C-defective V_8C_7 (JCPDS 00-035-0786) phases for both VC-1 and VC-2, being the VC-2 crystallinity lower than that of VC-1. The calculated crystallite sizes are 64 and 10 nm for VC-1 and VC-2, respectively. The TEM and HRTEM analyses in Figures 2A and 3A confirm the presence of smaller VC_x particles in VC-2 (mean size of 7.0 nm) than in VC-1 (mean size of 64.1 nm). In both cases, STEM-EDX analysis shows a homogeneous distribution of vanadium along the samples, see Figures 2B and 3B. VC-1 and VC-2 were analyzed in different zones by means of PED with spot electron diffraction-pattern recognition (PED-ASTAR). Experimental ED patterns of different zones were indexed according to V_8C_7 and VC, the best fitting indexation was used to obtain a reliable nanoscale phase mapping (Figures S4 and S5). In general, from PED-ASTAR analysis the major presence of VC phase can be deduced in VC-1, see Figure 2C. On the contrary, for VC-2, most of the analyzed zones showed a better fitting indexation when the presence of V_8C_7 is assumed, see Figure 3C.

Both samples show low intensity Raman bands centered at 1358 cm^{-1} and 1595 cm^{-1} (see Figure S6), reasonably assigned to the presence of residual amorphous carbon. Moreover, VC-1 shows several bands in the 100-1100 cm^{-1} region related to surface oxy-vanadium species, likely

formed when the samples were exposed to air [39-41]. The very low intensity band at 991 cm^{-1} indicates that, if any, the amount of crystalline V_2O_5 is very low [63-65]. The VC-2 presents much lower intense Raman bands in the 100-1100 cm^{-1} region than VC-1 (Figure S6), which would be related with the presence of a lower amount of surface oxy-vanadium species. The H_2-TPR profile of VC-1 (see Figure S7) indicates a small H_2 consumption at 743 K (0.77 mmol $H_2 \cdot g_{cat}^{-1}$), attributed to the reduction of mono-or polymeric oxy-vanadium (V) species; note that the reduction of amorphous V_2O_5 would take place at ~852 K and that of crystalline V_2O_5 at higher temperatures [64,66]. The low H_2 consumption (0.41 mmol H_2 g_{cat}^{-1}) of VC-2 at 528 K can be reasonably related to the reduction of vanadium oxycarbide species, as has been proposed for MoC_x systems [24].

The two catalysts were further analyzed by XPS. Figures 4A and 5A show the V 2p and C 1s core level spectra, respectively. The V 2p spectra can be deconvoluted into 3 doublets (V 2$p_{3/2}$ - V 2$p_{1/2}$). The analysis of V 2$p_{3/2}$ level with the corresponding bands centered at 513.6-513.8, 514.5-514.9, and 516.5-517.3 eV, clearly indicates the coexistence on the surface of vanadium carbide and different types of V^{n+}-O species, the latter corresponding to the two higher binding energy features [67-69]. The C 1s spectra of both VC-1 and VC-2 samples show a broad peak with maximum at 284.8 eV, the features at 282.9-283.0 eV are assigned to V-C species [67,68,70]; the shoulders at BE higher than 284.8 eV are related to the presence of C-O, C=O and O=C-O groups [71-73]. Consistent with this assignment, wide O 1s peaks were found (Figure S8A), being the component at lower BE (530.0-530.4 eV) assigned to oxy-species of vanadium and that at 531.3-531.5 eV to OH and/or oxycarbide species; components at higher BE are attributed to different oxygen-carbon bonded species [18,67,74]. On the other hand, XPS signals related to the presence of N-containing species were not found (Figure S9A), indicating that N coming from the 4,5-dicyanoimidazole used as C-precursor was eliminated during the VC_x preparation, discarding the presence of vanadium nitride species.

The CO_2 adsorption, which is a determining step of the RWGS, was studied on both samples, VC-1 and VC-2, by calorimetry. The experimental mean adsorption heat of CO_2 on VC-2 is -0.54 eV, much higher than on VC-1, having a value of -0.25 eV. Furthermore, the amount of CO_2 adsorbed on VC-2, 0.074 mg CO_2 mg_{cat}^{-1}, is slightly higher than that on VC-1, 0.059 mg CO_2 mg_{cat}^{-1}. Keeping in mind that the experimental mean adsorption heats involve a diversity of adsorptive situations, the experimental values of CO_2 adsorption heat correlate quite well with the DFT estimates of -0.85 and -0.18 eV for VC with C vacancy, VC-vac, and VC models, respectively (see Table S2 in Supplementary Material). In any case, the differences of adsorption heats seem to correlate well with VC-2 sample having much more C vacancies, which in turn corresponds with that of V_8C_7, than VC-1. In separate Thermogravimetric Analysis coupled to Mass Spectrometry

(TGA-MS) experiments, the reactivity of VC-1 and VC-2 with CO_2 at 873 K was followed for 3 h (Figure S10). Then, the catalysts were further analyzed by XRD (Figure S11). In both cases, CO_2 reacts with VC_x forming vanadium oxides and releasing CO.

The RWGS reaction was studied over VC-1 and VC-2 samples at 100 kPa, and temperatures ranging 573-873 K, using a $CO_2/H_2/N_2 = 1/3/1$ (in mols) reactant mixture under a GHSV of 3000 h^{-1}. Figure 6A shows the CO_2 conversion as a function of the reaction temperature, revealing a very low catalytic activity for both catalysts below 673 K. However, the CO_2 conversion increases with temperature reaching values of ~33% and 44% for VC-1 and VC-2 at 873 K, respectively. Besides CO, only CH_4 was formed. Both catalysts display a very high CO selectivity, increasing with temperature, see Figure 6B, with that of VC-2 being higher than that of VC-1. Consequently, the VC-2 CO yield is always higher than that of VC-1, while both increase with temperature (see Figure S12). The maximum CO yield is gained at 873 K on VC-2 being about 75 mol CO $kg_{cat}^{-1} \cdot h^{-1}$; at 873 K CH_4 selectivity is very low (< 0.05%). Taking into account that under the reaction conditions used, at temperatures lower than 873 K the methanation reaction is favored [75], it is noteworthy that even at 673 K over VC-2, a CH_4 selectivity of only 0.8% is found. The different characteristics of VC-1 and VC-2 are also reflected in the apparent activation energy for CO production, being 0.79 ± 0.04 eV and 0.55 ± 0.04 eV for VC-1 and VC-2, respectively, see Figure 7.

The above observed catalytic behaviour can be understood from the DFT-based calculations. We recall here that two systems are studied; the VC(001) surface, and the VC-vac derived from VC(001) with a surface C vacancy. The VC-vac is used for modeling the $V_8C_7(001)$ phase —see information on the validity of the model in the Experimental section and discussion in section S2 of the Supplementary Material. The adsorption of reactant and intermediate species for both the redox and the associative mechanisms have been acquired, and the PBE-D3 adsorption energies, including the ZPE term, are listed in Table S2 and depicted in Figures S13 and S14 of the Supplementary Material. Here, it is worth highlighting that the presence of C vacancies on VC makes it much more chemically active, with significant enhanced adsorption strength regardless of the species. Note that the adsorption strengthening is normally directly linked to the vacancy site itself (Figures S13 and S14) with the sole caveat of H_2, where the strongest site is the topM site *near* the vacancy, though. The different chemical activity introduced by the C vacancy becomes evident from the potential and Gibbs free energy profiles reported in Figure 8. The potential energy ($\Delta E^{\neq,ZPE}$) and Gibbs free energy ($\Delta G^{\neq}$) barriers —see conditions at S2 section in SI— for the different elementary steps are encompassed in Table 1, and the optimized geometries for the transition states are shown in Figures S15 and S16 of the Supplementary Material.

The potential energy diagram of the RWGS on VC shows low adsorption energies of CO_2 and H_2, and a moderate H_2 dissociation energy barrier of 0.84 eV, see Figure 8. The reaction mechanism can go either through the dissociative —CO_2 dissociation— or the associative mechanism —COOH formation. The common bifurcation point reveals a quite large energy barrier of 1.53 eV for CO_2 dissociation in an energy uphill process, and a lower energy barrier of 0.48 eV for the energy downhill COOH formation. However, the present calculations show that the immediately subsequent reaction step, this is, the COOH decomposition into CO + OH, is an uphill process with a high energy barrier of 1.59 eV, indicating that the redox mechanism is probably more affordable than the associative mechanism in VC. Indeed, dynamic aspects also would favour CO_2 dissociation since it is a unimolecular step, in principle faster than the associative COOH formation involving a bimolecular step. However, at present, it seems appropriate to consider that both mechanisms would be competitive on VC, although hardly achievable given their high-energy barriers.

The quite unfavourable situation for the RWGS on stoichiometric VC dramatically changes when the surface model involves carbon vacancies at the VC surface in a model mimicking the situation in the VC-2 sample. Here, the energy reaction profile shows significant variations with respect to that of the stoichiometric VC model. In particular, three critical points must be highlighted. First, the reactants adsorb much stronger, with adsorption energies being around three and five times larger for H_2 and CO_2 than on the stoichiometric surface, respectively (Table S2), and also higher than reported for transition metal catalysts, such as Ni(111), where the positive CO_2 adsorption energy becomes a drawback [76]. Second, the H_2 dissociation step is highly enhanced, becoming a highly downhill process, with an energy barrier of solely 0.16 eV, thus much reduced compared to the value of 0.65 eV of the VC (001) surface model, see Table 1, and of the order of H_2 dissociation on Ni(111) of 0.1 eV [77]. Finally, the RWGS mechanism gets unbalanced, in the sense that the redox route appears to be much favoured, being sensibly energetically downhill, and with a reduced energy barrier for CO_2 dissociation of 0.62 eV, which implies an impressive drop of 0.91 eV in such a rate-limiting reaction step, being also smaller than previous estimates of CO_2 dissociation on Ni(111), with computed values of 0.78 eV [76]. Furthermore, the associative mechanism becomes energetically uphill, with a much increased energy barrier, 1.20 eV compared to the 0.48 eV of the vacancy-free VC (001) surface, even though the following step, this is, the COOH decomposition into CO and OH, is here also greatly favoured, with an energy barrier of solely 0.38 eV, thus, much reduced compared to the vacancy-free VC case of 1.59 eV.

The Gibbs free-energy landscapes (at T = 873 K, p = 81.06 kPa, CO_2:H_2 = 1:3 and assuming 1% CO_2 conversion) mimic the potential energy ones, including the preference for the redox

11

mechanism for the model with C vacancies. The Gibbs free energy barriers are close to the ones corresponding to the potential energy profile, with no systematic deviations, which are, in average, of ~0.09 eV. Although $\Delta_r G^o$ at standard conditions is positive (like $\Delta_r E$), we have calculated and plotted in Figure 8 the reaction free energy assuming a 1% CO_2 conversion. This is a reasonable value given that in the fixed-bed reactor there is continuous flow of reactants, continuously impinging on the catalyst, where the heterogeneous reaction takes place and afterwards the final gas products leave the catalyst region. The negative value of $\Delta_r G^o$ indicates that, at these conditions the RWGS is to evolve spontaneously in the forward direction. On a more general overview of the full process, the VC carbide with surface C vacancies shows a profile with reactants, intermediates, and products close to zero Gibbs free energy, this is, adsorbing reactants, intermediates, and products moderately, and, therefore, being a better catalyst fulfilling *Le Sabatier* principle. Otherwise, if the material would adsorb reactants, intermediates, and products too weakly, such as in the defect-free VC, the profile is well above the zero energy, and the energetic cost prohibitive, and, on the other hand, if the material would adsorb such chemical moieties too strong, it would become self-poisoned by such. In summary, the presence of surface C vacancies largely favours the redox pathway, involving low-energy barriers, plus a moderate stabilization of reaction intermediates; both features explain the excellent capabilities of VC with C vacancies as a RWGS catalyst, which is fully consistent with the experimental results reported for the VC-2 sample with a larger content of C vacancies than VC-1. The theoretical calculations also explain the smaller apparent activation energy barrier estimated for the VC-2 sample, given that on VC(001) the rate-limiting step would feature an energy barrier of 1.41 eV, whereas it would drop to 0.48 eV for the VC-vac model, see Table 1. Our experimental and theoretical results suggest that under RWGS conditions the CO_2 dissociation takes place forming CO and O surface species, the later continuously react with H_2 forming H_2O. A similar reaction pathway has been proposed from experimental and theoretical studies for the RWGS over α-Mo_2C [24].

Last but not least, post-reaction VC-1 and VC-2 catalysts show no relevant structural changes occurred during the catalytic test according to XRD (see Figure S3) plus the VC_x crystallite size of post-reaction catalysts remains similar to that of the corresponding fresh catalysts. Furthermore, the V $2p$ and C $1s$ XPS spectra, see Figures 4B and 5B, respectively, indicate the presence of V−C species and an increase in the amount of oxy-vanadium species. The O $1s$ spectrum (see Figure S8B) shows that surface oxygen mainly forms oxy-vanadium and OH and/or oxycarbide species. These results suggest that the redox route dominate over both samples, in good agreement with the theoretical calculations. In order to check the stability of the VC-2 sample, which was the most efficient catalyst, a long-term catalytic test was carried out at 723 K for 4 days,

see Figure 9. Initially, during the first 4 h, CO_2 conversion slightly decreased and the CO selectivity slightly increased. After that, only a slight decrease on CO_2 conversion was observed till 30 h under reaction, meanwhile CO selectivity remained almost constant at 99.9%. No significant changes in the catalytic behavior of VC-2 were observed during the next 70 h. Clearly, the catalytic activity is marginally affected over reaction time, indirectly suggesting that the surface C vacancies are not remediated in the course of the reaction. The characterization of VC-2 after the long-term catalytic test using XRD (Figure S17) indicated a structural stability of the catalyst, meanwhile the presence of vanadium carbide species on the surface could be determined by XPS spectroscopy (Figure S18).

5. Conclusions

New synthetic approaches were used to obtain VC_x samples with different surface chemistry and catalytic behavior for the RWGS. Based on the results of a series of catalytic experiments, complementary characterization techniques, and DFT calculations, the present work provides compelling evidence that the presence of C vacancies in vanadium carbide leads to higher activity towards the RWGS reaction with an increased CO selectivity. This is a feature that may be engineered to increase/tune the catalytic activity and selectivity of transition metal carbides, in similar way it has been done for the surface chemistry and catalytic behavior of metal oxides in general [33,34], and for the RWGS catalyzed by supported gold catalysts, in particular [78].

The interpretation of the reported experiments is fully consistent with theoretical results analyzing in detail the molecular mechanism of the RWGS reaction on stoichiometric and C vacancy containing surface models. The calculations confirm that the presence of such vacancies is responsible for the observed catalytic behavior, featuring stronger adsorption energies for reactants —around three and five times larger for H_2 and CO_2—, and reducing the energy barrier for both H_2 and CO_2 dissociation steps, by ~0.5 and ~1 eV, respectively, plus the surface vacancy presence appears to be maintained during the reaction process.

To summarize, the present work highlights the importance of carbon vacancy native point defects in the general surface chemistry and catalytic properties of transition metal carbides and paves the way for improving the already high catalytic capability of these interesting materials.

Authors contributions
[¶]A. P. and H. P. contributed equally.

Appendix A. Supplementary Material

The following supplementary information related to this article can be found, in the online version, at DOI

S1. Vanadium carbide synthesis

S2. Validity of our computational model for V_8C_7

Figure S1. DFT optimized geometries for VC(001) with one surface C vacancy and V_8C_7(001)

Figure S2. DFT optimized geometries for CO_2 on VC(001) with one surface C vacancy and V_8C_7(001)

Table S1. DFT adsorption energies for CO_2 on VC(001) with one surface C vacancy and V_8C_7(001)

S3. Free energies

S4. Supplementary Figures

Figure S3. XRD patterns of fresh and post-RWGS catalysts

Figure S4. PED-ASTAR characterization of VC-1

Figure S5. PED-ASTAR characterization of VC-2

Figure S6. Raman spectra of VC-1 and VC-2

Figure S7. H_2-TPR profiles of VC-1 and VC-2

Figure S8. XPS profiles of O 1s level of VC-1 and VC-2

Figure S9. XPS profiles of N 1s level of VC-1 and VC-2

Figure S10. CO_2 reaction with catalysts followed by TGA-MS

Figure S11. XRD patterns of VC-1 and VC-2 catalysts after CO_2 treatment

Figure S12. CO production as a function of T over VC-1 and VC-2

S5. Supplementary Tables

References

Figure 1. Top view of the VC (left image) and VC-vac (right image) surface slab models. Black dots show the positions of the tested adsorption sites. V and C atoms are shown as light or dark grey spheres, respectively. The (2√2×2√2)R45º unit cell is shown with dashed lines.
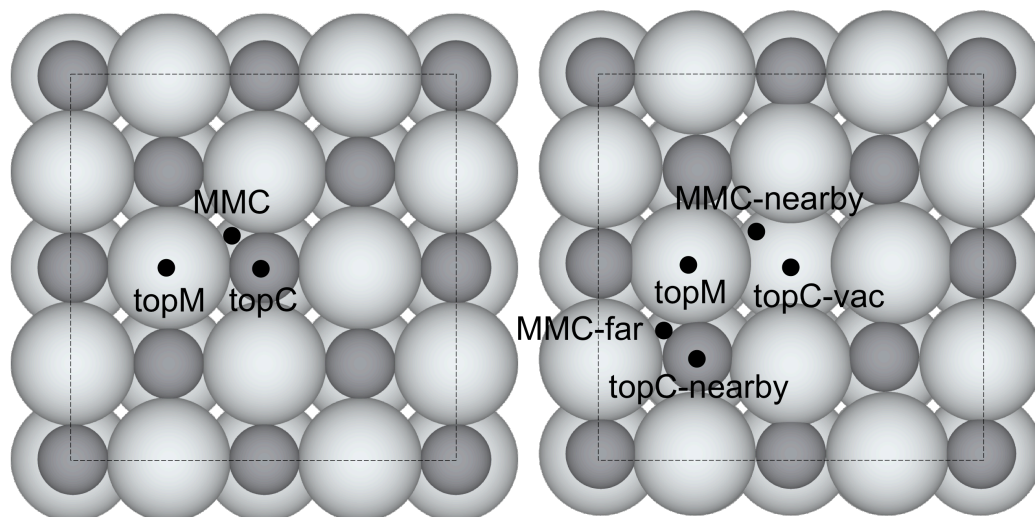
Figure 2. Characterization of VC-1: A) TEM images and particle size distribution; B) STEM image and vanadium EDX mapping combination; C) VC_x phase mapping determined by PED-ASTAR, see Figure S2 for the electron diffraction pattern and indexation used for phase mapping construction.
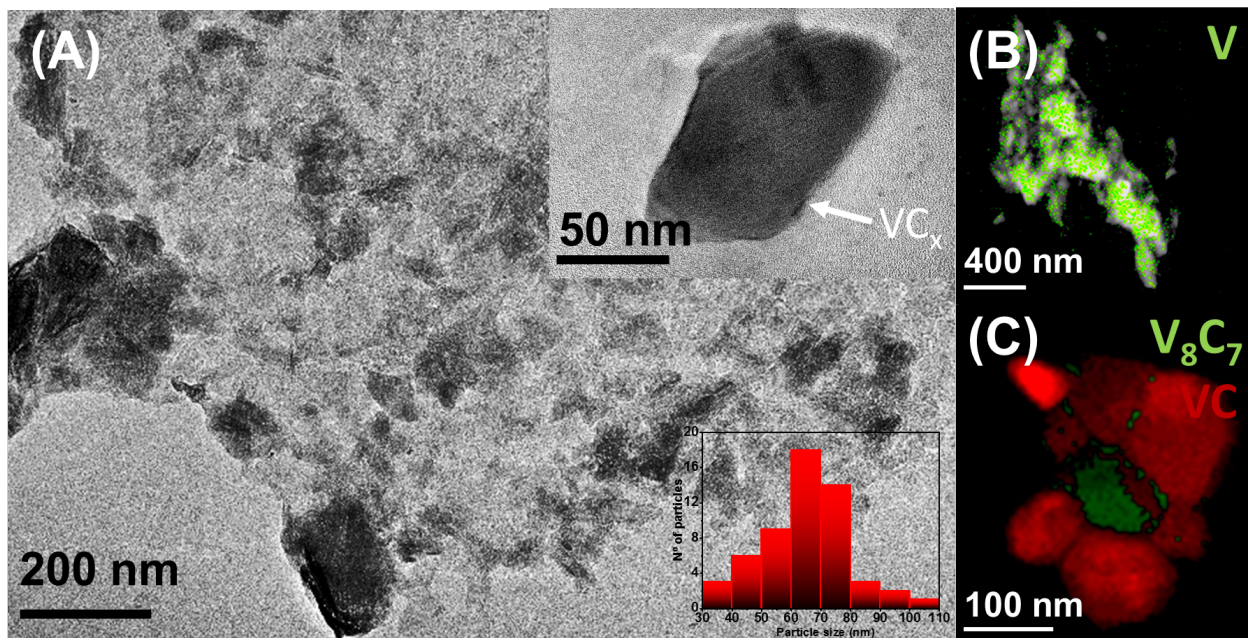
Figure 3. Characterization of VC-2: A) TEM and HRTEM images and particle size distribution; B) STEM image and vanadium EDX mapping combination; C) VC$_x$ phase mapping determined by PED-ASTAR, see Figure S3 for the electron diffraction pattern and indexation used for phase mapping construction.
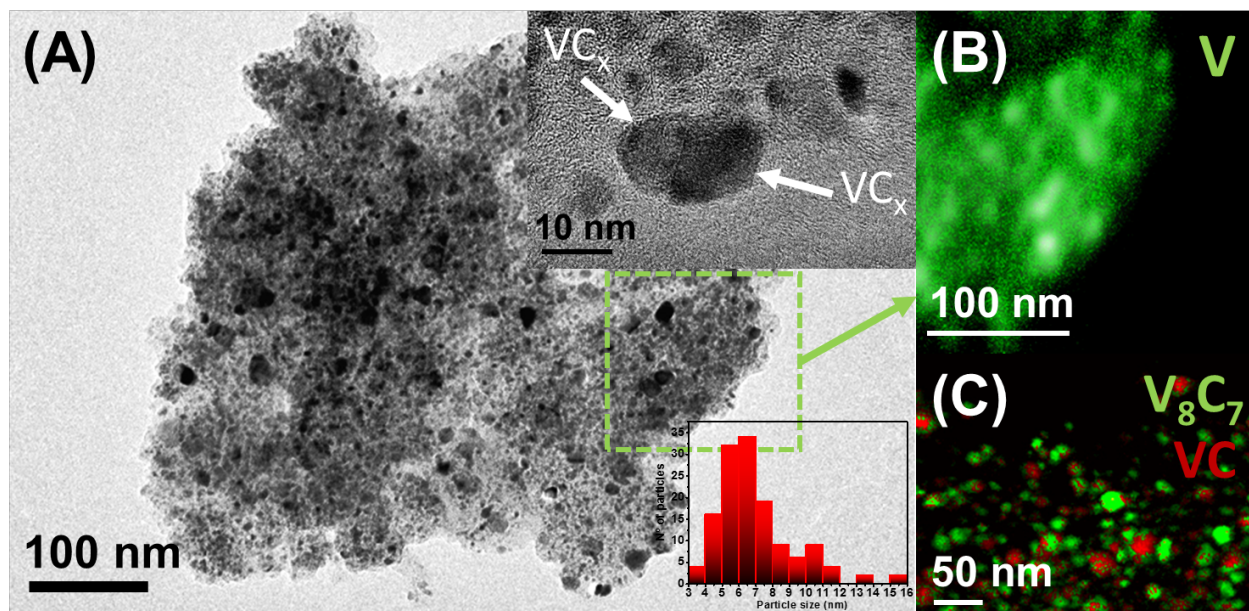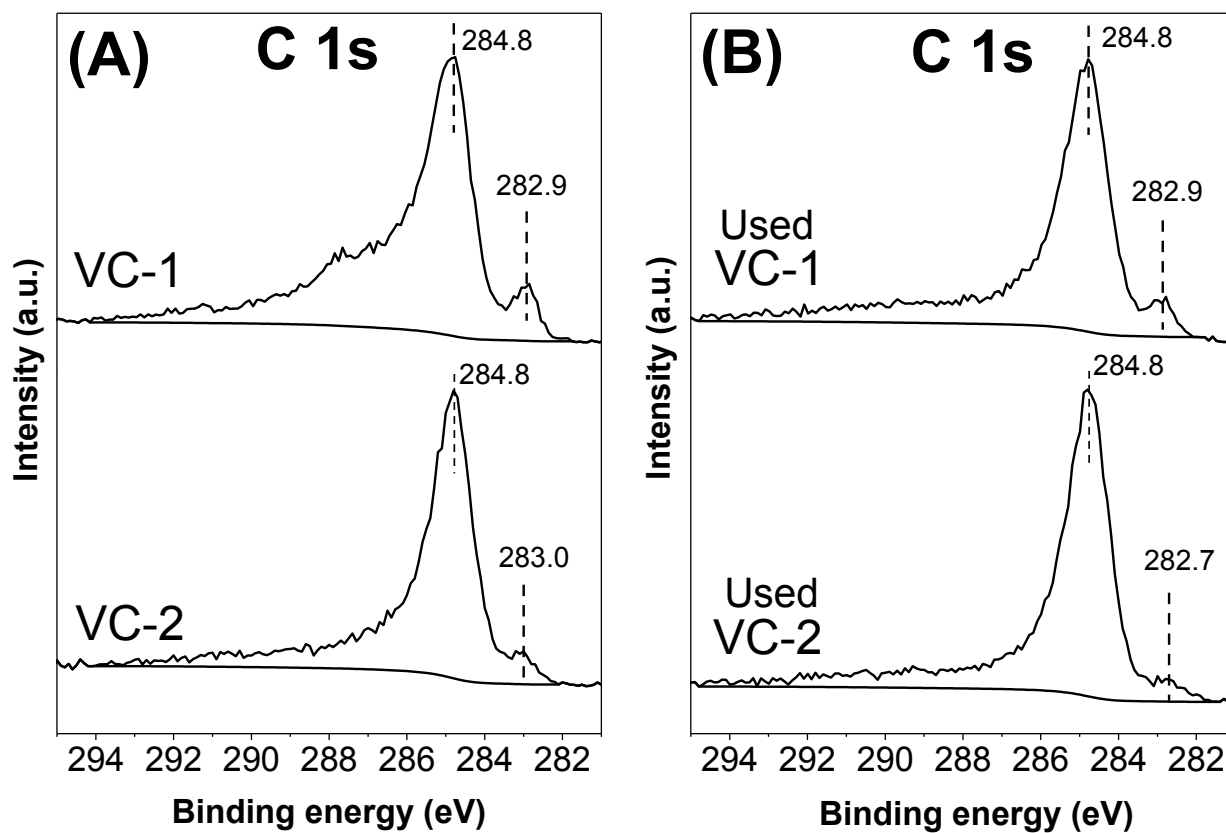
Figure 4. XPS profiles of V 2*p* levels of catalysts: A) fresh catalysts; B) after the RWGS catalytic tests.
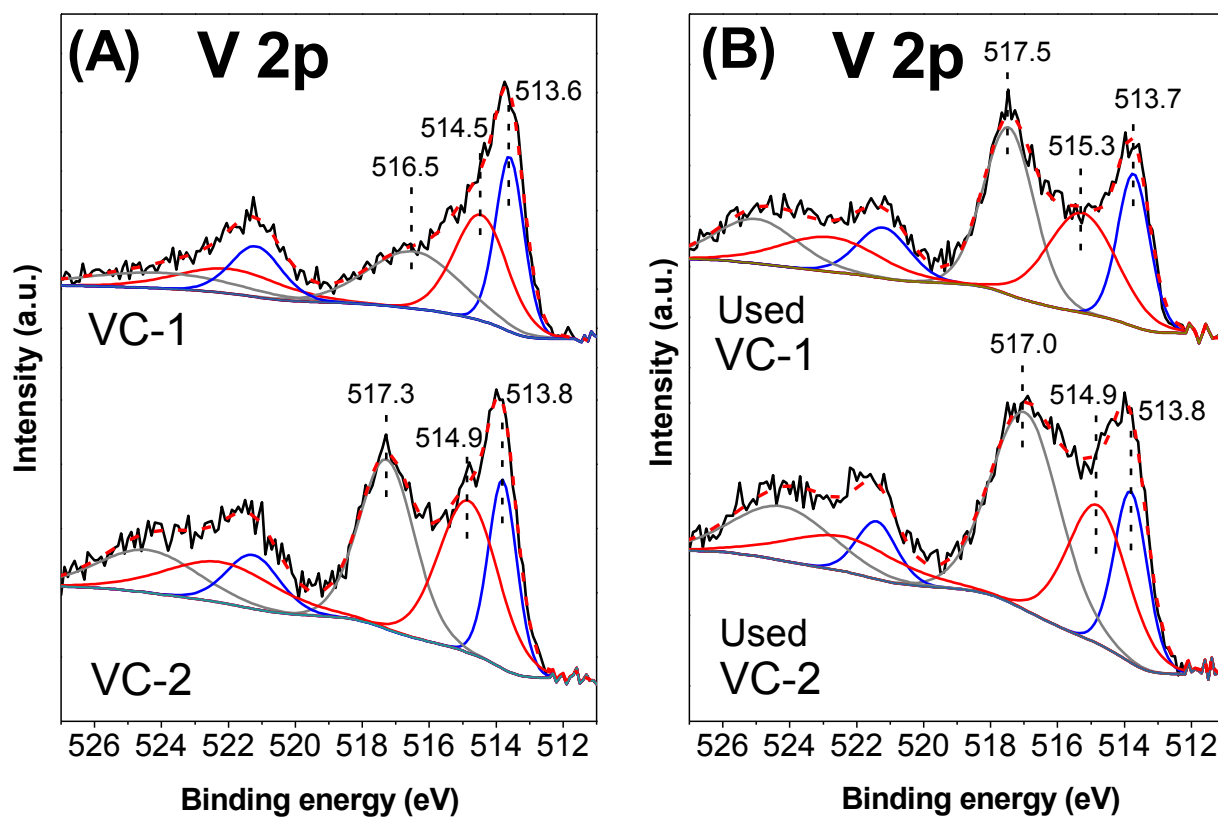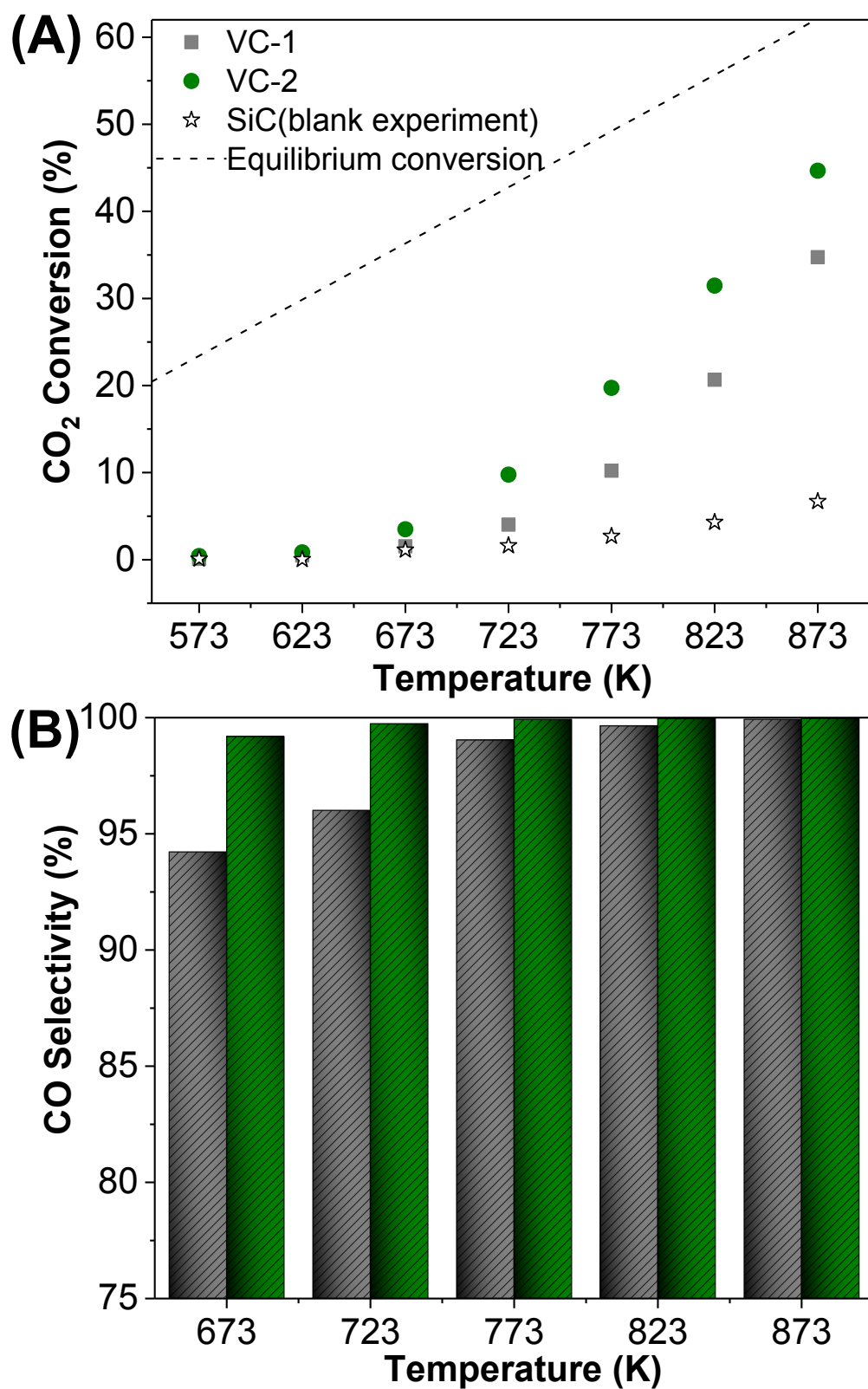
Figure 5. XPS profiles of C 1*s* level of catalysts: A) fresh catalysts; B) after the RWGS catalytic tests.
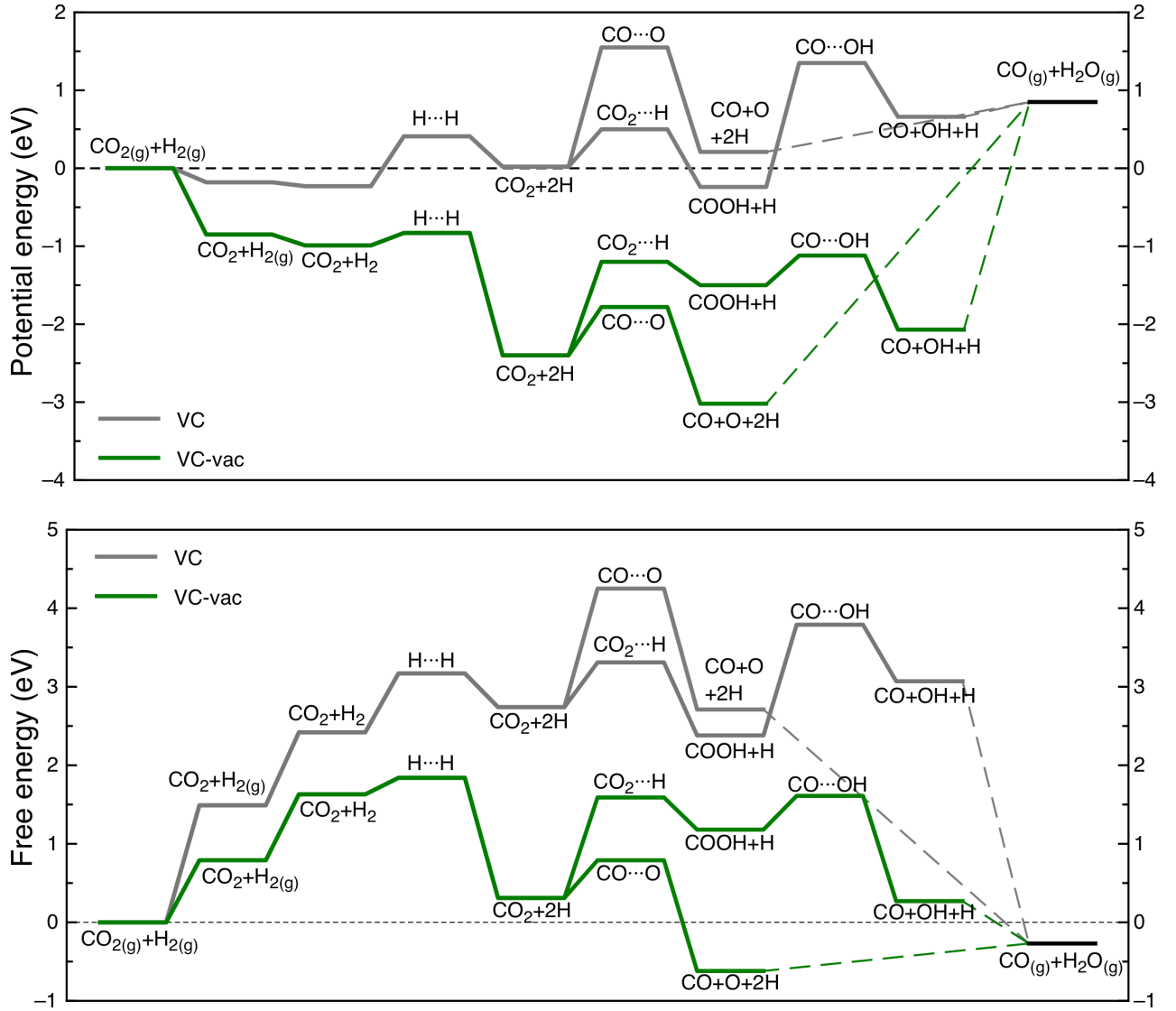
Figure 6. Catalytic behavior of VC-1 and VC-2 in the RWGS reaction as a function of reaction temperature: A) CO_2 conversion; B) CO selectivity, gray bars: VC-1 and green bars: VC-2. Reaction conditions: m_{cat} = 150 mg, $CO_2/H_2/N_2$ = 1/3/1, GHSV = 3000 h^{-1}, P = 0.1 MPa.

Figure 7. Apparent activation energy (E_a) for CO production over VC-1 and VC-2. Reaction conditions: m_{cat} = 150 mg, $CO_2/H_2/N_2$ = 1/3/1, GHSV = 3000 h^{-1}, p = 0.1 MPa, T = 723-873 K. The activation barriers found are 53.4±3.8 kJ mol-1 (0.55±0.04 eV) for VC-1, and 76.5±4.0 (0.79±0.04 eV) for VC-2.
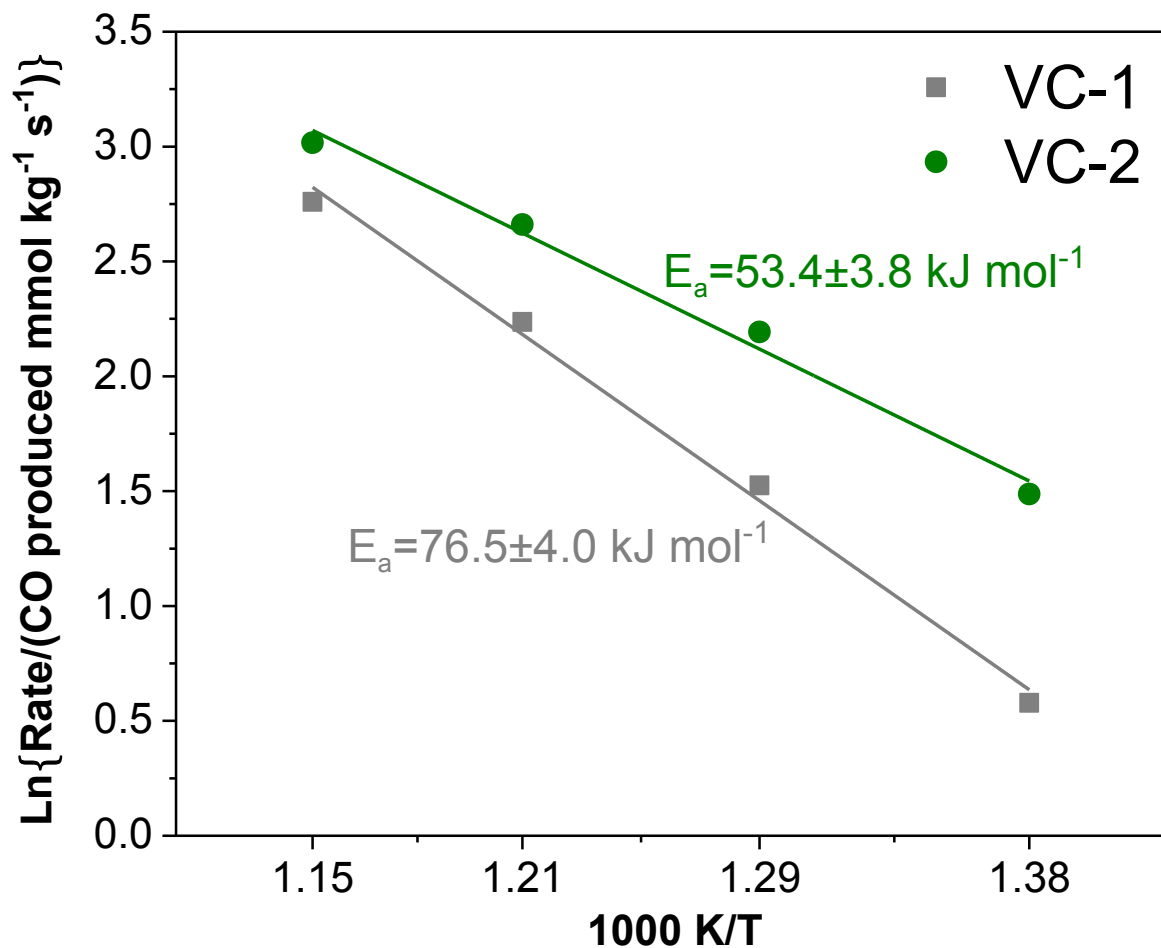
Figure 8. Upper panel: Potential energy reaction profiles (PBE-D3 including the ZPE term) for the RWGS on the VC (001) surface (grey) and on the VC-vac (001) surface model (green). Lower panel: Equivalent Gibbs free energy reaction profiles at $T = 873$ K, $p_{CO_2} = 20.26$ kPa, $p_{H_2} = 60.79$ kPa, and $p_{CO} = p_{H_2O} = 0.20$ kPa.

Figure 9. Catalytic behavior of VC-2 in RWGS at 723 K as a function of time on stream: CO_2 conversion and CO selectivity. Reaction conditions: m_{cat} = 300 mg, $CO_2/H_2/N_2$ = 1/3/1, GHSV = 3000 h^{-1}, p = 0.1 MPa.
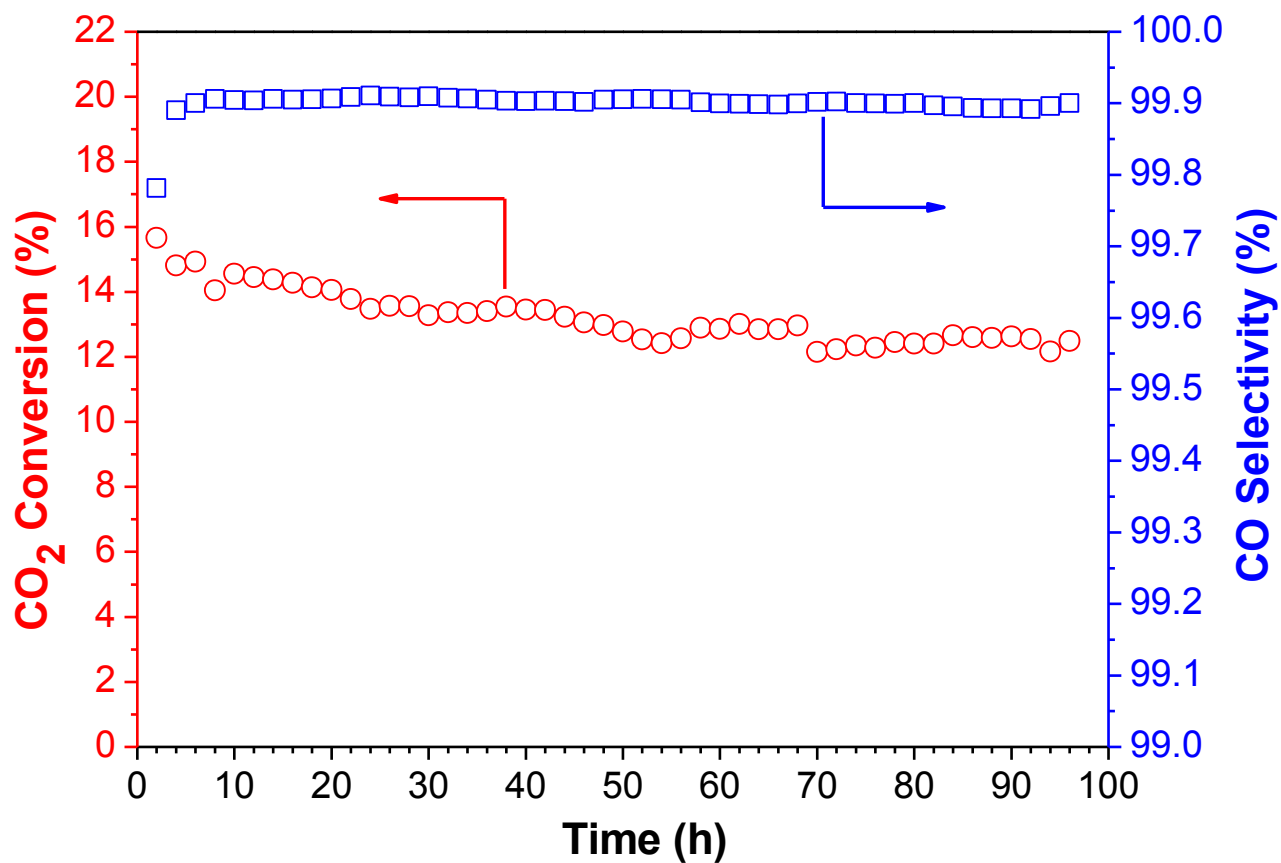
Table 1. Potential ($\Delta E^{\neq,ZPE}$) and free energy ($\Delta G^{\neq}$) barriers for different elementary steps of the RWGS on the (001) surface models of VC, and of the same surface containing a surface C vacancy (VC-vac). All values are ZPE-corrected and have been obtained at the PBE-D3 level. The Gibbs free energy values are gained at $T = 873$ K, $p_{CO_2} = 20.26$ kPa, $p_{H_2} = 60.79$ kPa, and $p_{CO} = p_{H_2O} = 0.20$ kPa.

Reaction Step	$\Delta E^{\neq,ZPE}$ / eV		$\Delta G^{\neq}$ / eV	
	VC	VC-vac	VC	VC-vac
$H_2 \rightarrow 2H$	0.65	0.16	0.74	0.21
$CO_2 \rightarrow CO+O$	1.53	0.62	1.51	0.48
$CO_2+H \rightarrow COOH$	0.48	1.20	0.57	1.29
$COOH \rightarrow CO+OH$	1.59	0.38	1.41	0.43

References

[1] W. Taifan, J.-F. Boily, J. Baltrusaitis, Surface chemistry of carbon dioxide revisited. Surf. Sci. Rep. 71 (2016) 595–671.

[2] D.Y.C. Leung, G. Caramanna, M.M. Maroto-Valer, An overview of current status of carbon dioxide capture and storage technologies. Renew. Sustain. Energy Rev. 39 (2014) 426-443.

[3] D.M. D'Alessandro, B. Smit, J.R. Long, Carbon dioxide capture: Prospects for new materials. Angew. Chem. Int. Ed. 49 (2010) 6058–6082.

[4] M.E. Boot-Handford, J.C. Abanades, E.J. Anthony, M.J. Blunt, S. Brandani, N. Mac Dowell, J.R. Fernández, M.-C. Ferrari, R. Gross, J.P. Hallett, R.S. Haszeldine, P. Heptonstall, A. Lyngfelt, Z. Makuch, E. Mangano, R.T.J. Porter M. Pourkashanian, G.T. Rochelle, N. Shah, J.G. Yao, P. S. Fennell, Carbon capture and storage update. Energy Environ. Sci. 7 (2014) 130–189.

[5] P. Markewitz, W. Kuckshinrichs, W. Leitner, J. Linssen, P. Zapp, R. Bongartz, A. Schreiber, T.E. Müller, Worldwide innovations in the development of carbon capture technologies and the utilization of CO_2. Energy Environ. Sci. 5 (2012) 7281-7305.

[6] M.W. Chase Jr., NIST-JANAF Thermochemical Tables. 4th Edition, J. Phys. Chem. Ref. Data, Monograph 9, 1-1951, 1998.

[7] C. Graves, S.D. Ebbesen, M. Mogesen, K.S. Lackner, Sustainable hydrocarbon fuels by recycling CO_2 and H_2O with renewable or nuclear energy. Renew. Sustain. Energy Rev. 15 (2011) 1–23.

[8] W. Wang, S. Wang, X. Ma, J. Gong, J. Recent advances in catalytic hydrogenation of carbon dioxide. Chem. Soc. Rev. 40 (2011) 3703-3727.

[9] C. Kunkel, F. Viñes, F. Illas, Transition metal carbides as novel materials for CO_2 capture, storage, and activation. Energy Environ. Sci. 9 (2016) 141–144.

[10] R.B. Levy, M. Boudart, Platinum-like behavior of tungsten carbide in surface catalysis. Science 181 (1973) 547–549.

[11] H.H. Hwu, J.G. Chen, Surface chemistry of transition metal carbides. Chem. Rev. 105 (2005) 185–212.

[12] J.A. Rodriguez, P. Liu, J. Dvorak, T. Jirsak, J. Gomes, Y. Takahashi, K. Nakamura, Adsorption of sulfur on TiC(001): Photoemission and first-principles studies. Phys. Rev. B 69 (2004) 115414.

[13] A.R.S. Darujati, D.C. LaMont, W.J. Thomson, Oxidation stability of Mo_2C catalysts under fuel reforming conditions. J. Appl. Catal. A 253 (2003) 397–407.

[14] P. Liu, J.A. Rodriguez, J.T. Muckerman, Sulfur adsorption and sulfidation of transition metal carbides as hydrotreating catalysts. J. Mol. Catal. A 239 (2005) 116–124.

[15] D.J. Sajkowski, S.T. Oyama, Catalytic hydrotreating by molybdenum carbide and nitride: unsupported Mo_2N and Mo_2C/Al_2O_3. Appl. Catal. A 134 (1996) 339-349.

[16] C. Kunkel, F. Viñes, F. Illas, Biogas upgrading by transition metal carbides. ACS Appl. Energy Mater. 1 (2018) 43–47.

[17] T. Takahashi, S. Sutherland, A. Kozyr, Global ocean surface water partial pressure of CO_2 database: Measurements performed during 1957–2017, Environmental Sciences Division, Oak Ridge National Laboratory, 2018.

[18] C. Kunkel, F. Viñes, P.J. Ramírez, J.A. Rodriguez, F. Illas, Combining theory and experiment for multitechnique characterization of activated CO_2 on transition metal carbide (001) surfaces. J. Phys. Chem. C 123 (2019) 7567-7576.

[19] J.J. Piñero, P.J. Ramírez, S.T. Bromley, F. Viñes, F. Illas, J.A. Rodriguez, Diversity of adsorbed hydrogen on the TiC (001) surface at high coverages. J. Phys. Chem. C 122 (2018), 28013-28020.

[20] S. Posada-Pérez, F. Viñes, R. Valero, J.A. Rodriguez, F. Illas, Adsorption and dissociation of molecular hydrogen on orthorhombic β-Mo_2C and Cubic δ-MoC (001) surfaces. Surf. Sci. 656 (2017) 24-32.

[21] H. Prats, J.J. Piñero, F. Viñes, S.T. Bromley, R. Sayós and F. Illas, Assessing the usefulness of transition metal carbides for hydrogenation reactions. Chem. Comm. 55 (2019) 12797-12800.

[22] S. Posada-Pérez, F. Viñes, J.A. Rodriguez, F. Illas, Fundamentals of methanol synthesis on metal carbide based catalysts: Activation of CO_2 and H_2. Top. Catal. 58 (2015) 159-173.

[23] A. Goguet, F. Meunier, J.P. Breen, R. Burch, M.I. Petch, A. Faur Ghenciu, Study of the origin of the deactivation of a Pt/CeO_2 catalyst during Reverse Water Gas Shift (RWGS) reaction. J. Catal. 226 (2004) 382–392.

[24] X. Liu, C. Kunkel, P. Ramírez de la Piscina, N. Homs, F. Viñes, F. Illas, Effective and highly selective CO generation from CO_2 using a polycrystalline α-Mo_2C catalyst. ACS Catal. 7 (2017) 4323–4335.

[25] M.D. Porosoff, S. Kattel, W. Li, P. Liu, J.G. Chen, Identifying trends and descriptors for selective CO_2 conversion to CO over transition metal carbides. Chem. Commun. 51 (2015) 6988−6991.

[26] M. D. Porosoff, X. Yang, J.A. Boscoboinik, J.G. Chen, Molybdenum carbide as alternative catalysts to precious metals for highly selective reduction of CO_2 to CO. Angew. Chem. 126 (2014) 6823−6827.

[27] S. Posada-Pérez, F. Viñes, P.J. Ramírez, A.B. Vidal, J.A. Rodriguez, F. Illas, The bending machine: CO_2 activation and hydrogenation on δ-MoC(001) and β-Mo_2C(001) surfaces. Phys. Chem. Chem. Phys. 16 (2014) 14912-14921.

[28] S. Posada-Pérez, P.J. Ramirez, J. Evans, F. Viñes, P. Liu, F. Illas, J.A. Rodriguez, Highly active Au/δ-MoC and Cu/δ -MoC catalysts for the conversion of CO_2: The metal/C Ratio as a key factor defining activity, selectivity, and stability. J. Am. Chem. Soc. 138 (2016) 8269-8278.

[29] S. Posada-Pérez, R.A. Gutierrez, Z.J. Zuo, P.J. Ramirez, F. Viñes, P. Liu, F. Illas, J. Rodriguez, Highly active Au/δ-MoC and Au/β-Mo_2C catalysts for the low-temperature water gas shift reaction: Effects of the carbide metal/carbon ratio on the catalyst performance. Catal. Sci. Technol. 7 (2017) 5332-5342.

[30] H. Fang, A. Roldan, C. Tian, Y. Zheng, X. Duan, K. Chen, L. Ye, S. Leoni, Y. Yuan, Structural and catalysis of tungsten carbides for the regioselective cleavage of C-O bonds, J. Catal. 369 (2019) 283-295.

[31] Y. Zhang, B. Liu, J. Wang, Self-assembly of carbon vacancies in sub-stoichiometric ZrC_{1-x}. Sci. Rep. 5 (2015) 18098.

[32] H.W. Hugosson, P. Korzhavyi, U. Jansson, B. Johansson, O. Eriksson, Phase stabilities and structural relaxations in sub-stoichiometric TiC_{1-x}. Phys. Rev. B 63 (2001) 165116.

[33] G. Pacchioni, Oxygen vacancy: The invisible agent on oxide surfaces. ChemPhysChem 4 (2003) 1041-1047.

[34] C.T. Campbell, C.H.F. Peden, Oxygen vacancies and catalysis on ceria surfaces. Science 309 (2005) 713-714 and references therein.

[35] S.J. Tauster, S.C. Fung, R.L. Garten, Strong metal-support interactions - Group-8 noble-metals supported on TiO_2. J. Am. Chem. Soc. 100 (1978) 170-175.

[36] S.J. Tauster, S.C. Fung, R.T.K. Baker, J.A. Horsley, Strong-interactions in supported-metal catalysts. Science 211 (1981) 1121-1125.

[37] W. Dong, Q. Fu, Z. Jiang, B. Mei, X. Bao, Carbide-supported Au catalysts for water-gas shift reactions: A new territory for the strong metal-support interaction Effect. J. Am. Chem. Soc. 140 (2018) 13808-13816.

[38] J.R. Kitchin, J.K. Nørskov, M.A. Barteau, J.G. Chen, Trends in the chemical properties of early transition metal carbide surfaces: A density functional study. Catal. Today 105 (2005) 66-73.

[39] Y.F. Zhang, F. Viñes, Y.J. Xu, Y. Li, J.Q. Li, F. Illas, Role of kinetics in the selective surface oxidations of transition metal carbides. J. Phys. Chem. B 110 (2006) 15454-15458.

[40] F. Viñes, C. Sousa, F. Illas, P. Liu, J.A. Rodriguez, Density functional study of the adsorption of atomic oxygen on the (001) surface of early transition-metal carbides. J. Phys. Chem. C 111 (2007) 1307-1314.

[41] F. Viñes, C. Sousa, F. Illas, P. Liu, J.A. Rodriguez, A systematic density functional study of molecular oxygen adsorption and dissociation on the (001) surface of group IV−VI transition metal carbides. J. Phys. Chem. C 111 (2007) 16982-16989.

[42] X. Peng, L. Hu, L. Wang, X. Zhang, J. Fu, K. Huo, L.Y.S. Lee, K.-Y. Wong, P.K. Chu, Vanadium carbide nanoparticles encapsulated in graphitic carbon network nanosheets: A high-efficiency electrostatic for hydrogen evolution reaction. Nano Energy 26 (2016) 603-609.

[43] C. Giordano, C. Erpen, W. Yao, B. Milke, M. Antonietti, Metal nitride and metal carbide nanoparticles by a soft urea pathway. Chem. Mater. 21 (2009) 5136-5144.

[44] X. Liu, A. Pajares, D.J.D. Calinao Matienzo, P. Ramírez de la Piscina, N. Homs, Preparation and characterization of bulk Mo_xC catalysts and their use in the reverse water-gas shift reaction. Catal. Today, DOI: 10.1016/j.cattod.2019.11.011.

[45] M. Nagai, K. Oshikawa, T. Kurakami, T. Miyao, S. Omi, Surface properties of carbided molybdena–alumina and its activity for CO_2 hydrogenation. J. Catal. 180 (1998) 14-23.

[46] W. Wu, Z. Wu, C. Liang, X. Chen, P. Ying, C. Li, In Situ FT-IR Spectroscopic studies of CO adsorption on fresh Mo_2C/Al_2O_3 Catalyst. J. Phys. Chem. B 107 (2003) 7088-7094.

[47] W. Wu, Z. Wu, C. Liang, P. Ying, Z. Feng, C. Li, An IR study on the surface passivation of Mo_2C/Al_2O_3 catalyst with O_2, H_2O and CO_2. Phys. Chem. Chem. Phys. 6 (2004) 5603-5608.

[48] D. Viladot, M. Véron, M. Gemmi, F. Peiró, J. Portillo, S. Estradé, J. Mendoza, N. Llorca-Isern, S. Nicolopoulos, Orientation and phase mapping in the transition electron microscope using precession-assisted diffraction spot recognition: State-of-the-art results. J. Microsc. 252 (2013) 23-34.

[49] E.F. Rauch, M. Véron, Automated crystal orientation and phase mapping in TEM. Mater. Charact. 98 (2014) 1-9.

[50] S. Rouvimov, E.F. Rauch, P. Moeck, S. Nicolopoulos, Automated crystal orientation and phase mapping of iron oxide nano-crystals in a transmission electron microscope. Microsc. Microanal. 15 (2009) 1290-1291.

[51] G. Kresse, J. Furthmüller, Efficient iterative schemes for ab initio total-energy calculations using a plane-wave basis set. Phys. Rev. B 54 (1996) 11169–11186.

[52] J.P. Perdew, K. Burke, M. Ernzerhof, Generalized gradient approximation made simple. Phys. Rev. Lett. 77 (1996) 3865–3868.

[53] S. Grimme, J. Antony, S. Ehrlich, H. Krieg, A consistent and accurate ab initio parametrization of density functional dispersion correction (DFT-D) for the 94 elements H-Pu. J. Chem. Phys 132 (2010) 154104.

[54] P.E. Blöchl, Projector augmented-wave method. Phys. Rev. B 50 (1994) 17953–17979.

[55] G. Kresse, D. Joubert, From ultrasoft pseudopotentials to the projector augmented-wave method. Phys. Rev. B 59 (1999) 1758–1775.

[56] H.J. Monkhorst, J.D. Pack, Special points for Brillouin-zone integrations. Phys. Rev. B 13 (1976) 5188–5192.

[57] M.G. Quesne, A. Roldan, N.H. Leeuw, C.R.A. Catlow, Bulk and surface properties of metal carbides: Implications for catalysis. Phys. Chem. Chem. Phys. 20 (2018) 6905–6916.

[58] F. Viñes, J.R.B. Gomes, F. Illas, Understanding the reactivity of metallic nanoparticles: beyond the extended surface model for catalysis. Chem. Soc. Rev. 43 (2014) 4922–4939.

[59] G. Henkelman, B.P. Uberuaga, H. Jónsson, A climbing image nudged elastic band method for finding saddle points and minimum energy paths. J. Chem. Phys. 113 (2000) 9901–9904.

[60] A. Hjorth Larsen, J. Jørgen Mortensen, J. Blomqvist, I.E. Castelli, R. Christensen, M. Dułak, J. Friis, M.N. Groves, B. Hammer, C. Hargus, E.D. Hermes, P.C. Jennings, P.B. Jensen, J. Kermode, J.R. Kitchin, E.L. Kolsbjerg, J. Kubal, K. Kaasbjerg, S. Lysgaard, J.B. Maronsson, T. Maxson, T. Olsen, L. Pastewka, A. Peterson, C. Rostgaard, J. Schiøtz, O. Schütt, M. Strange, K.S. Thygesen, Vegge, L. Vilhelmsen, M. Walter, Z. Zeng, K.W. Jacobsenet, The atomic simulation environment – A Python library for working with atoms. J. Phys. Condens. Matter 29 (2017) 273002.

[61] S. Smidstrup, A. Pedersen, K. Stokbro, H. Jónsson, Improved initial guess for minimum energy path calculations. J. Chem. Phys. 140 (2014) 214106.

[62] J. Rogal, K. Reuter, Ab initio atomistic thermodynamics for surfaces: A primer in experiment, modeling and simulation of gas-surface interactions for reactive flows in hypersonic flights. Educational notes. Neuilly-sur- Seine, France (2007).

[63] F. Roozeboom, M.C. Mittelmeijer, J.A. Moulijn, J. Medema, V.H.J. De Beer, P.J. Gellings, Vanadium oxide monolayer catalysts. 3. A Raman spectroscopic and temperature-programmed reduction study of monolayer and crystal-type vanadia on various supports, J. Phys. Chem. 84 (1980) 2783-2791.

[64] G. Liu, Z.-J. Zhao, T. Wu, L. Zeng, J. Gong, Nature of the active sites of VO_x/Al_2O_3 catalysts for propane dehydrogenation. ACS Catal. 6 (2016) 5207-5214.

[65] D.A. Bulushev, L. Kiwi-Minsker, F. Rainone, A. Renken, Characterization of surface vanadia forms on V/Ti-Oxide catalyst via temperature-programmed reduction in hydrogen and spectroscopic methods, J. Catal. 205 (2002) 115-122.

[66] F. Arena, F. Frusteri, A. Parmaliana, Structure and dispersion of supported-vanadia catalysts. Influence of the oxide carrier, Appl. Catal. A. 176 (1999) 189-199.

[67] J.-G. Choi, The surface properties of vanadium compounds by X-Ray photoelectron spectroscopy, Appl. Surf. Sci. 148 (1999) 64-72.

[68] M.C. Biesinger, L.W.M. Lau, A.R. Gerson, R.St.C. Smart, Resolving surface chemical states in XPS analysis of first row transition metals, oxides and hydroxides: Sc, Ti, V, Cu and Zn. Appl. Surf. Sci. 257 (2010) 887-898.

[69] G. Silversmit, D. Depla, H. Poelman, G.B. Marin, R.D. Gryse, Determination of the V2p XPS binding energies for different vanadium oxidation states (V^{5+} to V^{0+}). J. Electron. Spectros. Relat. Phenomena 135 (2004) 167-175.

[70] S. Kaur, G. Cherkashinin, C. Fasel, H.J. Kleebe, E. Ionescu, R.J. Riedel, Single-source-precursor synthesis of novel V_8C_7/SiC(O)-based ceramic nanocomposites. J. Eur. Ceram. 36 (2016) 3553-3563.

[71] D. Yang, A. Velamakanni, G. Bozoklu, S. Park, M. Stoller, R.D. Piner, S. Stankovich, I. Jung, D.A. Field, C.A. Ventrice Jr., R.S. Ruoff, Chemical analysis of graphene oxide films after chemical treatments by X-ray photoelectron and micro-Raman spectroscopy. Carbon 47 (2009) 145-152.

[72] Y. Sun, X. Hu, W. Luo, Y. Huang, Ultrafine MoO_2 nanoparticles embedded in carbon matrix as a high-capacity and long-life anode for lithium-ion bateries. J. Mater. Chem. 22 (2012) 425-431.

[73] M. Chen, J. Liu, W. Zhou, J. Lin, Z. Shen, Nitrogen-doped graphene-supported transition-metals carbide electrocatalysts for oxygen reduction reaction. Sci. Rep. 5 (2015) 10389-10399.

[74] A. Bhaskar, M. Deepa, T.N. Rao, MoO_2/multiwalled carbon nanotubes (MWCNT) hybrid for use as a Li-Ion Battery Anode. ACS Appl. Mater. Interfaces. 5 (2013) 2555-2566.

[75] P. Kaiser, R.B. Unde, C. Kern, A. Jess, Production of liquid hydrocarbons with CO_2 as carbon source based on reverse water-gas shift and Fischer-Tropsch synthesis. Chem. Ing. Tech. 85 (2013) 489-499.

[76] S.-G. Wang, D.-B. Cao, Y.-W. Li, J. Wang, H. Jiao, CO_2 reforming of CH_4 on Ni(111): A density functional theory calculation. J. Phys. Chem. B 110 (2006) 9976-9983.

[77] A.H. Zhang, J. Zhu, W.H. Duan, Study of dissociation barriers of H_2 on Ni(111) and Ni_3Fe(111). Phys. B 393 (2007) 223-227.

[78] L.F. Bobadilla, J.L. Santos, S. Ivanova. J.A. Odriozola, A. Urakawa Unravelling the role of oxygen vacancies in the mechanism of the reverse Water–Gas Shift reaction by operando DRIFTS and Ultraviolet–Visible Spectroscopy. ACS Catal. 2018, 88, 7455-7467.